J Solid State Electrochem (2018) 22:835–847
https://doi.org/10.1007/s10008-017-3813-y

ORIGINAL PAPER

Synthesis and electrochemical investigation of spinel cobalt ferrite magnetic nanoparticles for supercapacitor application

H. Kennaz [1] · A. Harat [1] · O. Guellati [1,2] · D. Y. Momodu [3] · F. Barzegar [3] · J. K. Dangbegnon [3] · N. Manyala [3] · M. Guerioune [1]

Received: 14 November 2016 / Revised: 18 October 2017 / Accepted: 18 October 2017 / Published online: 4 November 2017

Abstract Cobalt ferrite magnetic nanoparticles ($CoFe_2O_4$-MNPs) were synthesized by hydrothermal and co-precipitation methods using different precursors such as nitrates, chlorides, and acetates, at different concentrations with/without surfactant under different growth conditions. The structural and morphological analyses reveal the formation of a single-phase $CoFe_2O_4$ in nanoplatelet-shaped NPs with average particle size between 11 and 26 nm depending on synthesis condition. The specific surface area of these NPs obtained by hydrothermal method was ~ 34 $m^2\ g^{-1}$. Electrochemical performances of the obtained nanoparticles in a three-electrode configuration with a 6 M KOH electrolyte revealed a specific capacitance (C_s) of 429 F/g at 0.5 A/g, with excellent capacitance retention of 98.8% after 6000 cycles at 10 A/g for the electroactive NPs synthesized by hydrothermal method at 200 °C for 18 h.

Keywords Cobalt ferrite MNPs · Co-precipitation · Hydrothermal synthesis · Coercive field · Magnetization · Supercapacitor

Introduction

Magnetic ferrite nanoparticles have shown a growing interest in recent years due to their exceptional physical and chemical properties with potential applications in chemical sensors, catalysts, ferrofluids [1], spintronics, and medicine [2–4]. In addition to these applications, there is equally an increasing interest in energy storage research based on the fast growing market for electronic devices which are being designed to be smaller, lighter, and relatively cheaper. Thus, an all-in-one device requires efficient energy storage components which will fit into such design blueprint with improved energy performance.

Electrochemical capacitors (ECs, also known as supercapacitors) have gained a rapidly growing attention over the past years due to their potential suitability for the ongoing technological advancement in electronic devices as well as their capability to deliver high specific power as compared to batteries [5]. Supercapacitors (SCs), besides being environmentally friendly, also exhibit remarkable properties such as long cycle life and rapid charge-discharge rate. Although their specific energy densities are still currently lower than high-performance batteries, there is still an ongoing study to improve the energy density of supercapacitors through research into novel materials for energy storage.

SCs can be classified into two basic types according to their charge storage mechanism, as follows: the electric double-layer capacitors (EDLCs) where electrode material is mainly carbonaceous in nature with charge storage based on the accumulation of ions at the electrode/electrolyte interface and faradaic capacitors, consisting of metal oxides/conducting polymer electrode materials which generate fast reversible redox reactions. Till date, a wide range of materials have been investigated as electrodes for SC

✉ A. Harat
harat_aicha@yahoo.fr; aicha.harat@univ-annaba.dz

[1] LEREC Laboratory, Physics Department, Badji Mokhtar-Annaba University, BP.12, 23000 Annaba, Algeria

[2] Fac. Sci, Université Mohamed Cherif Messadia de Souk Ahras, BP. 1553, 41000 Souk Ahras, Algeria

[3] Department of Physics, Institute of Applied Materials, SARChI Chair in Carbon Technology and Materials, University of Pretoria, Pretoria 0028, South Africa

application [5, 6]. Among these, faradaic active SC materials like the transition metal oxides, such as Co_3O_4, NiO, MnO_2, and Fe_2O_3 [7–10], have been reported to exhibit remarkably high specific capacitance and excellent reversibility, with some of the oxides combined to form metal-oxide/carbon composites showing a remarkable enhancement of the electrochemical properties [11, 12]. Spinel ferrites MFe_2O_4 (M = Fe, Cu, Ni, Co, etc.) and their related nanocomposites have been adopted as potential materials both in Li-ion battery and SC applications [13–15]; particularly, cobalt ferrite has received renewed attention for its remarkable properties such as strong anisotropy, high saturation magnetization and coercivity, reasonable cost, shape versatility, and high chemical and structural stability at higher temperatures [16, 17]. The methods widely used for the synthesis of magnetic cobalt ferrite include thermal decomposition of a mixed Co^{2+}–Fe^{3+} oleate complex [18], hydrothermal synthesis [19–22], sonochemical reactions [23], synthesis in oil-in-water micelles [24], aqueous co-precipitation and calcination [25–27], combustion, host template [28], microwave plasma, forced hydrolysis in a polyol medium, flow injection synthesis [29], spray drying, and sol–gel processing [30]. Even though most of these methods are cost effective, some of them however involve longer preparation times due to the multiple steps that need to be followed.

The hydrothermal route (a low-temperature growth process at around 200 °C) is one of the commonly used growth routes, owing to its economic advantage and high degree of compositional control [21]. Also, co-precipitation of iron and cobalt ions in alkaline medium (usually NaOH) has proven to be a convenient and inexpensive synthesis route suitable for producing large batches of materials with a reasonable control of the composition and particle size. Consequently, the optimization of the synthesis parameters, such as temperature, time, and molarity, can lead to a better regulation of particle morphology, specific surface area, and pore size distribution of the material which in turn influences the improvement of their electrochemical properties.

In the present paper, the synthesis of cobalt ferrite magnetic nanoparticles ($CoFe_2O_4$-MNPs) is described by two different synthesis methods involving "chemical co-precipitation and hydrothermal methods." This is done by utilizing different precursors such as nitrates, chlorides, and acetates at different concentrations with and without the presence of a surfactant, under different growth conditions of time and temperature. The electrochemical capacitance behavior of the best samples (with optimized growth condition for both methods) has been studied. The results show the achievement of a considerably high specific capacitance value and excellent cycle performance for these cobalt ferrite products which make them good candidates as electrodes for SC application.

Experimental and characterization

$CoFe_2O_4$ MNP synthesis

Cobalt nitrate (99.0%), cobalt chloride (99.0%), cobalt acetate (99.0%), iron nitrates (99.1%), iron chloride (99.0%), sodium hydroxide (97.0%), and polyethylene glycol (PEG-400) are purchased from Biochem Chemopharma. Potassium hydroxide (85–100.5%) and carbon black are purchased from Sigma-Aldrich.

Electro-active materials were obtained by both co-precipitation and hydrothermal methods as follows.

Co-precipitation method

Cobalt–ferrite nanoparticles were obtained using different precursors: chlorides, chloride-acetate, nitrates, and chlorides with surfactant-based sources denoted Cp-Cl, Cp-Cl/Ac, Cp-N, and Cp-Cl/surf, respectively. Synthesis was carried out according to the following steps:

- Chloride-based sources (Cp-Cl): 50 ml of 0.08 M $FeCl_3 \cdot 6H_2O$ and 50 ml of 0.04 M $CoCl_2 \cdot 6H_2O$ solutions were mixed in distilled water (with atomic ratio Fe/Co = 2:1). The resulting solution was added drop-wise to a 100-ml solution of 0.64 M NaOH. Afterwards, the resultant solution was kept at 45 °C for 2 h under vigorous stirring.
- Chloride–acetate-based source (Cp-Cl/Ac): 25 ml of 0.04 M $FeCl_3 \cdot 6H_2O$ and 25 ml of 0.02 M $Co(CH_3COO)_2 \cdot 4H_2O$ solutions were mixed in distilled water. The resulting solution was added drop-wise to a 50-ml solution of 0.32 M NaOH. The synthesis temperature was maintained at 45 °C for 2 h under vigorous stirring.
- Nitrate-based sources (Cp-N): 100 ml of 0.2 M $Fe(NO_3)_3 \cdot 9H_2O$ and 100 ml of 0.1 M $Co(NO_3)_2 \cdot 6H_2O$ solutions were mixed in distilled water. Then, 100 ml solution of 3 M NaOH was added drop by drop in the first solution. Subsequently, the resulting solution in this case was stirred at 80 °C for 2 h. Finally, a quantity of this obtained powder (Cp-N) was calcined in an oven at 300 °C for 2 h and was denoted as Cp-N/cal.
- Chloride-based sources with surfactant (Cp-Cl/surf): 25 ml of 0.4 M $FeCl_3 \cdot 6H_2O$ and 0.2 M of $CoCl_2 \cdot 6H_2O$ solutions were mixed in distilled water. The resulting solution was added drop-wise to an 80-ml solution of 0.8 M NaOH. Then, the obtained solution was kept at 80 °C for 30 min under vigorous stirring. Later, 2 ml of polyethylene glycol (PEG) was added drop by drop in the last solution, as surfactant, under stirring at 100 °C for 1 h.

For all synthesis reactions, the pH was done in the range of 12–12.6, and at the end of each process, the obtained solution was filtrated and washed several times with deionized water, then the collected powders were dried in an oven at 80 °C overnight.

Hydrothermal method

Cobalt ferrite MNPs were synthesized using a simple and low-cost hydrothermal method. Firstly, an aqueous solution is made by mixing 10 ml of 1 M $Fe(NO_3)_3·9H_2O$ to 10 ml of 0.5 M $Co(NO_3)_2·6H_2O$ (with atomic ratio Fe/Co = 2:1). Then, a solution of 10 ml of 6 M NaOH was directly added to the mixture. The final solution was kept under vigorous magnetic stirring for 30 min and was transferred into a Teflon-lined stainless steel autoclave which was placed in a preheated oven at 200 °C for different growth times. The autoclave was naturally cooled down to room temperature. The solution was filtered and washed several times with deionized water. The collected powder was dried at 80 °C overnight. The obtained samples were named H-1M-1h and H-1M-18h for 1 and 18 h growth durations, respectively. Following the same steps described above, samples H-0.1M-1h and H-0.1M-18h were also synthesized by varying the molarity of the precursors (i.e., 0.1 and 0.05 M for Fe and Co-based nitrates, respectively).

Structural and morphological characterization

X-ray diffraction (XRD) patterns were collected using an X′ Pert PRO diffractometer (PANalytical BV, Netherlands) with theta/2theta geometry, operating with Cu-K_α source. The SEM micrographs of the samples were obtained using a Zeiss Ultra Plus 55 Field Emission Scanning Electron Microscope (FE-SEM) operated at an accelerating voltage of 2.0 kV. Transmission electron microscopy (TEM) was carried out with a JEOL JEM-2100F microscope operated at 200 kV (Akishima-shi, Japan). Nitrogen adsorption–desorption isotherms were measured at − 196 °C temperature using liquid nitrogen with a Micromeritics TriStar II 3020 (Version 2.00). Impurities and moisture were removed from the sample surfaces by degassing at 180 °C for 12 h under vacuum. The surface area was obtained with the Brunauer–Emmett–Teller (BET) method. The Barrett–Joyner–Halenda (BJH) method was used to determine the pore size distribution of the samples from the desorption branch of the isotherm. Raman spectroscopy measurements were carried out using a Jobin Yvon Horiba TX 6400 micro-Raman spectrometer equipped with a triple monochromator system to eliminate contributions from Rayleigh lines. All the samples were excited with the 514-nm line of an argon laser with a laser power of 1.5 mW. Fourier transform infrared (FTIR) spectra were recorded using a Bruker Vertex 77v FTIR spectrometer (in a wavenumber range of 400 to 4000 cm^{-1}).

Magnetic measurements

Magnetic characterization was performed using a Quantum Design MPMS superconducting quantum interference device (SQUID) magnetometer. Zero field-cooled (ZFC) and field-cooled (FC) measurements of magnetization were performed at applied magnetic fields of 5 and 50 mT in the temperature range from 4 to 300 K. Magnetic field dependence of magnetization was measured at applied magnetic field up to 5 T at 300 K.

Working electrode preparation and electrochemical measurements

All the working electrodes (WE) were composed of known masses of synthesized electro-active materials, carbon black as conductive additive, and polyvinylidene fluoride (PVdF) as binder agent with a mass ratio of 80:10:10, respectively. The active materials were carefully dispersed in N-methylpyrrolidone (NMP) solution to form slurry which was pasted onto 1-cm^2-area Ni-foam current collectors. The obtained working electrode (WE) was dried at 60 °C in an electric oven overnight. In this way, complete evaporation of the NMP is assured. The active material consists of the nanoparticles of co-precipitation (Cp-N) and hydrothermal (H-1M-18h) samples. In a three-electrode configuration, electrochemical measurements (ECs) were carried out with 6 M KOH as electrolyte and glassy carbon plate and Ag/AgCl (3 M KCl) as the counter and the reference electrode, respectively. All EC measurements such as cyclic voltammetry (CV), chronopotentiometry (CP), and electrochemical impedance spectroscopy (EIS) tests were performed using a Bio-Logic VMP-300 potentiostat. The CV tests were carried out in the potential range of 0 to 0.4 V at different scan rates ranging from 5 to 100 mV/s. Electrochemical impedance spectroscopy (EIS) measurements were performed with an open circuit potential and over a frequency range from 100 kHz to 10 mHz.

Results and discussion

Structural and microstructural analysis

Figure 1a, b shows the XRD patterns of the as-synthesized ferrite samples analyzed with the MAUD program (version 2.33) [31]. The diffraction peaks in the 2θ range of 10°–80° correspond to the characteristic reflections of the cubic spinel structure (space group Fd3m, n°227). As an example, the best Rietveld refinement of the XRD pattern of the H-1M-18h sample is represented in Fig. 1c where experimental points are represented by the blue color and the fitted profile by the black color, as well as the subtraction in the window below.

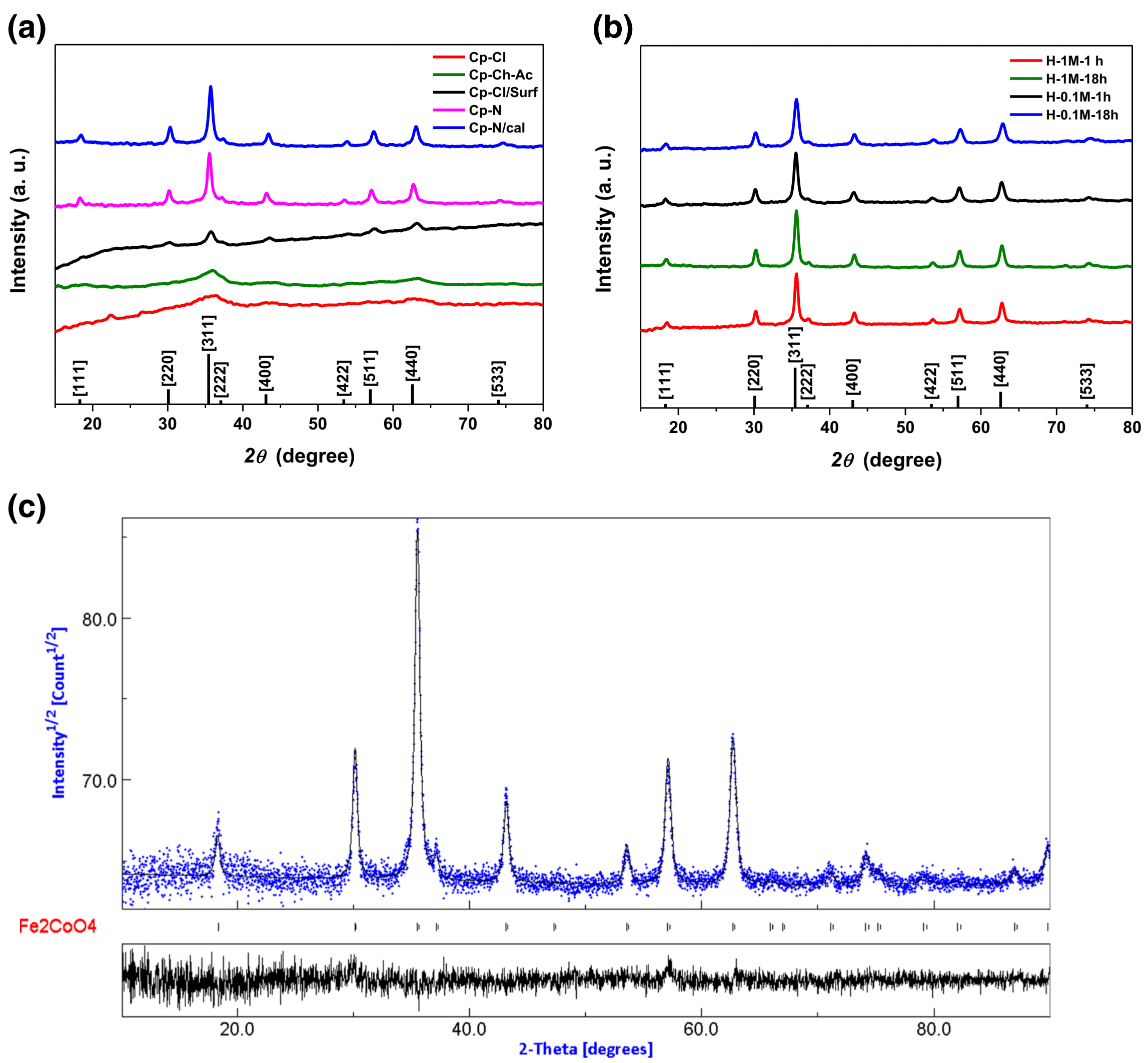

Fig. 1 XRD patterns of $CoFe_2O_4$ MNPs prepared by **a** co-precipitation and **b** hydrothermal methods. **c** Rietveld refinement of H-1M-18h sample spectra

No additional phase was detected justifying the synthesis structural selectivity.

The fitting results of the lattice parameter and the crystallite size are summarized in Table 1; the results are in agreement with the standard JCPDS card No. 22-1086 for Co ferrite.

From Fig. 1a, for the samples prepared by the co-precipitation method, the appearance of only three broadening spinel phase peaks (311), (400), and (440) for the Cp-Cl and Cp-Cl-Ac samples can be attributed to the amorphous state and/or to the small particle size of the as-prepared samples; this can be explained by the low growth temperature condition. Additional peaks belonging to the spinel phase appear with the addition of the PEG surfactant at synthesis temperature of 100 °C for the Cp-Cl/surf sample. These results are similar to those reported in the previous study [32] which show that the cubic spinel crystallization process begins to appear at 40 °C and is complete at 80 °C for chloride-based precursors. Thus, it can be stated that the presence of the PEG surfactant aids in the process of crystallization along with the reduction of crystallite size. However, all the phase peaks appear and become sharper for nitrate precursor samples which indicate the good crystallization of products.

Table 1 Structural parameters of the obtained cobalt ferrite MNPs

Method/sample		Lattice parameter A (Å)	Crystallite size D (nm)
Co-precipitation	Cp-N	8.3701	19.08
	Cp-N/cal	8.3380	19.84
	Cp-Cl	–	–
	Cp-Cl/surf	8.3296	11.15
	Cp-Cl-Ac	–	–
Hydrothermal	H-1M-1h	8.3669	26.57
	H-1M-18h	8.3795	18.12(17[a])
	H-0,1M-1h	8.3770	21.67
	H-0,1M-18h	8.3598	19.83(19[a])

[a] Crystallite size from HRTEM micrographs

Figure 1b shows the XRD spectra of the samples prepared by the hydrothermal method. It is clear that there is no obvious difference between the obtained spectra and the strong diffraction peaks reveal the high crystallinity of products while the large peak width is attributed to the nanoscale particle size. Moreover, no significant effect was observed with the change of the concentration and reaction time. More interestingly, it is observed that the $CoFe_2O_4$ pure phase has directly been successfully obtained without any calcination steps for both co-precipitation and hydrothermal methods.

From Table 1, the lattice parameter (denoted as a) of samples made by different methods is similar. However, a decrease in the lattice parameter of the calcined sample (Cp-N/cal) is observed as compared to Cp-N, which could be attributed to an increased degree of inversion [33]. As such, with the increase of temperature, the migration of the Co^{2+} cation in the tetrahedral and octahedral sites favors the lattice expansion, which results in the decrease of the lattice parameter [34]. The lattice parameter for the Cp-Cl/surf sample was also significantly smaller. This can also be attributed to the modification of the cationic repartition of Co^{2+} and Fe^{3+} on the octahedral and tetrahedral sites [35, 36].

The FESEM and TEM micrographs of the synthesized cobalt ferrite MNPs using co-precipitation and hydrothermal methods are shown Fig. 2. The particle size is rather smaller for this sample as compared to the others coupled with a large agglomeration of the nanoparticles even with the addition of a surfactant (Cp-Cl/surf sample) which makes the specific morphology and particle sizes not easily observable. However, the HRTEM micrographs in Fig 2f, g show that the samples are composed of nanoplatelets (square-shaped nanoparticles) with narrow particle size distribution.

The average size obtained by counting 220 nanoparticles as shown in the histogram represented in Fig. 2h was found to be around 17 nm for the H-1M-18h sample which is in agreement with the Rietveld refinement from the XRD analysis.

The gas sorption analysis with N_2 adsorption–desorption isotherms which is used to measure the specific surface area (SSA) by the BET method and the desorption isotherms of Barrett–Joyner–Halenda (BJH) plots of the pore size distribution (PSD) of H-1M-18h and Cp-N samples are shown in Fig. 3. According to the IUPAC classification [37], the obtained hysteresis plots belong to the group of type IV isotherms. The SSA_{BET}, average pore size, and pore volume of the two samples are respectively 34.22 m^2/g, 3.48 nm, and 0.0873 cm^3/g, for the H-1M-18h sample, and 20.81 m^2/g, 3.33 nm, and 0.1142 cm^3/g, for the Cp-N sample. As shown from the desorption pore volume plot in the inset of Fig. 3, pore size belongs to a narrow range: 2–10 nm for the H-1M-18h sample and 1.45–10 nm for Cp-N samples, which is associated to the porous nature of materials exhibiting a narrow distribution of relatively uniform mesopores.

Figure 4a shows the Raman spectra of H-1M-1h and H-0.1M-18h samples. For the cobalt ferrite, there are five Raman active modes expected: $A_g + E_g + 3T_{2g}$. The spectra of the two samples reveal the presence of peaks at 543 and 663 cm^{-1} related to the T-site mode that reflects the local lattice effect in the tetrahedral sub-lattice; other peaks at 190, 283, and 460 cm^{-1} correspond to the O-site mode that reflects the local lattice effect in the octahedral sub-lattice. This is consistent with the previously reported studies [38, 39]. The five Raman active modes which are expected for the cubic inverse-spinel ferrite system are visible in the spectra. FT-IR spectroscopy is a very useful technique to explain the position of the surface groups in the crystal structure and their vibration modes. For the ferrite particles, this technique can offer information about redistribution of cations between octahedral and tetrahedral sites of the inverse spinel structure. FT-IR spectra of Cp-N and H-1M-18h samples recorded in the range 390–4000 cm^{-1} are shown in Fig. 4b. The bands with the higher wavenumber observed in the range of 550–600 cm^{-1} corresponds to intrinsic stretching vibrations of the metal at the tetrahedral site [40], whereas the others bands in the range 400–468 cm^{-1} are attributed to the octahedral metal stretching confirming the formation of inverse spinel $CoFe_2O_4$ nanoferrites [41].

Magnetic properties

Magnetic measurements were done for the H-1M-18h sample prepared by the hydrothermal method. It was cooled in a zero magnetic field, and then zero field-cooled (ZFC) magnetization was measured by increasing the temperature in an applied field of 50 and 500 Oe. For the field-cooled (FC) protocol, the sample was also cooled in the same fields and then the magnetization was recorded with increasing temperature in the range 4–300 K. The curves in Fig. 5a show the irreversibility in the measured temperature range which is atypical behavior of super-paramagnetic particles. The ZFC curve shows a gradual increase without any notable maximum in the measured range. Moreover, the curves do not overlap at 300 K indicating that the blocking temperature, T_B, tends to shift toward the high-temperature region showing a larger T_B in the Co ferrite NPs, (i.e., beyond 300 K), and this is comparable with the results obtained in previous studies for $CoFe_2O_4$ NPs [42–44]. This observation may be attributed to different aspects: Firstly, the large particle size distribution causes the broadening of the transition to the super-paramagnetic state toward higher temperatures. Secondly, there would be clustering occurring on powder samples which is associated to a strong dipolar or even exchange interactions between particles [45]. It was also discovered that the FC curves decrease when lowering the temperature in the thermal range of 300–180 K indicating also a super-spin glass behavior caused by a strong inter-particle dipolar interaction [46].

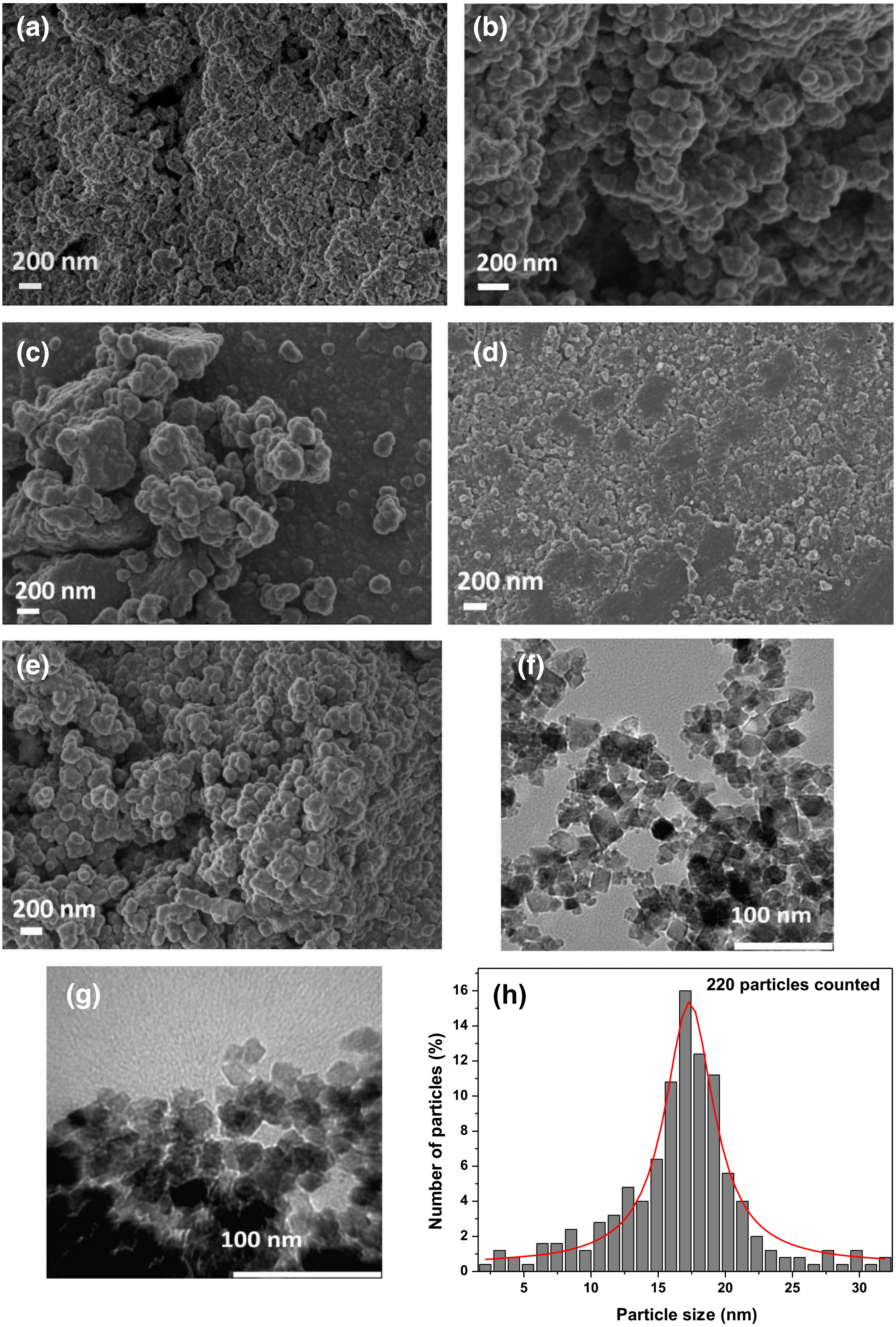

Fig. 2 FESEM micrographs of **a** Cp-N, **b** Cp-N/cal, **c** Cp-Cl/Ac, **d** Cp-Cl/surf, and **e** H-1M-18h samples. TEM micrographs of **f** H-1M-18h and **g** H-0.1M-18h samples. **h** Particle size distribution of the H-1M-18h sample

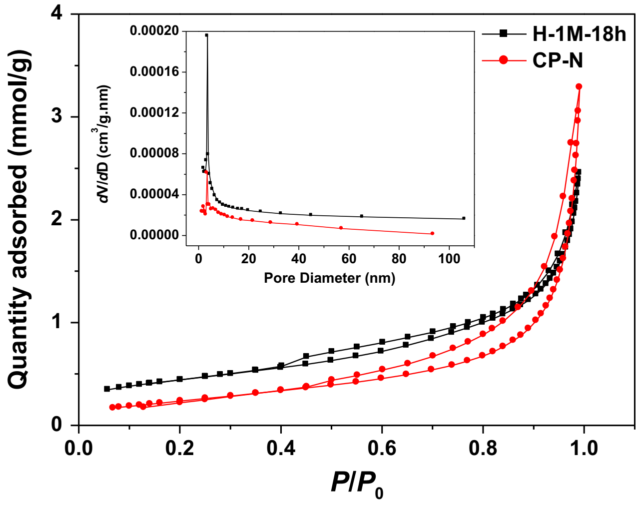

Fig. 3 N_2 adsorption–desorption isotherms of H-1M-18h and Cp-N simples and the corresponding pore size distribution from the BJH desorption (inset)

The M (H) loop at room temperature is represented in Fig. 5b. The extrapolated magnetic parameters such as saturation magnetization M_s, remanent magnetization M_r, and coercive field H_c are 63.5 emu/g, 46.7 emu/g, and 750 Oe, respectively. The M_s value is lower than the bulk $CoFe_2O_4$ value (75.2 emu/g) [47] which is attributed to the small particle surface effect (spin canting) that becomes more dominant as the particles are smaller. The obtained values of M_s and H_c are comparable to values obtained for similar particle sizes in the previous study [48]. However, comparison with the literature on such spinel systems shows that these parameters are not only particle size-dependent but also dependent on the elaboration method. For example, in the table summary on the study by Rao et al. [49], the difference could be attributed to the degree of inversion of the spinel phase, i.e., the position of magnetic atoms on the lattice.

Electrochemical analysis

Electrochemical performances of the two samples synthesized by co-precipitation (Cp-N) and hydrothermal (H-1M-18h) methods were tested. Figure 6a shows the cyclic voltammograms (CV) of the H-1M-18h sample measured at different potential ranges at 20 mV/s scan rate. From the shape and cycle area, one can easily state that the $CoFe_2O_4$ material can be considered as a good electrode in the positive potential range with $E_{we} < 0.5$ V in 6 M KOH electrolyte. Figure 6b shows the CV curves of the H-1M-18h sample recorded within the potential range of 0–0.4 V at different scan rates. We see the appearance of the typical peaks due to the occurrence of faradaic redox reactions. The obvious increase in current density with scan rates indicates the good rate capability and capacitance behavior. In Fig. 6c, a comparison between CV curves of H-1M-18h and Cp-N electrodes are shown at a scan rate 20 mV/s; one can notice the larger integrated area and current density for cobalt ferrites obtained by hydrothermal process as compared to that synthetized by the co-precipitation method. The specific capacitance C_s of the two electrodes was calculated using the following relation:

$$C_s = \frac{\int i \, dV}{m \, \nu \Delta V} \tag{1}$$

where i is the current, ΔV is the potential window, m is the mass of the active material pasted on the Ni-foam current collector, and ν is the potential scan rate.

C_s values of 315 and 249 F/g were obtained for the H-1M-18h and Cp-N samples, respectively, at the scan rate of 5 mV/s. These values are of the same order of magnitude, which is realistic considering their specific surface area values (see Table 1). Moreover, the C_s values of our products are larger than those obtained for pure cobalt ferrite materials of previous studies [50, 51] (see Table 2), which is attributed to the

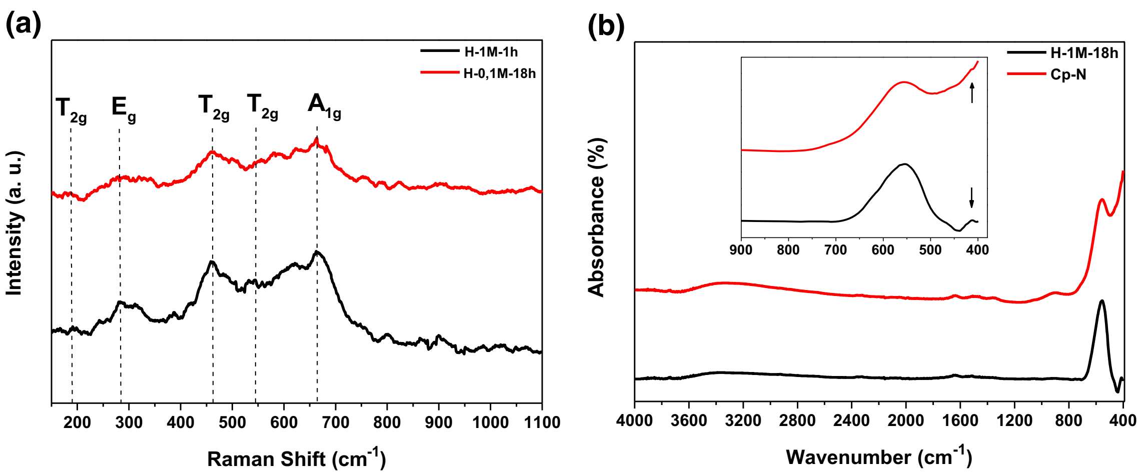

Fig. 4 **a** Raman spectra of H-1M-1h and H-1M-18h samples. **b** FTIR spectra of H-1M-18h and Cp-N samples

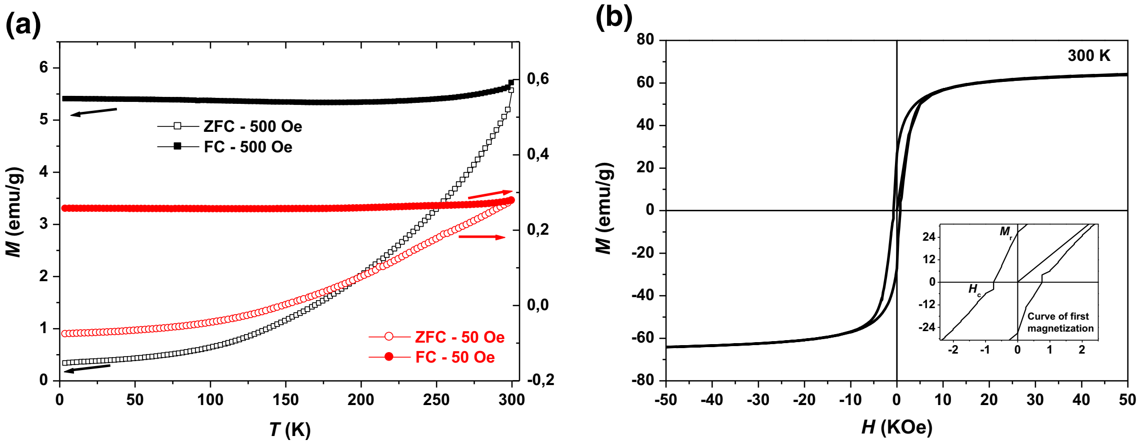

Fig. 5 **a** Temperature dependence of zero field cooled (ZFC) and field cooled (FC) at applied magnetic fields of 50 and 500 Oe. **b** Magnetic hysteresis loops at 300 K of the H-1M-18h sample

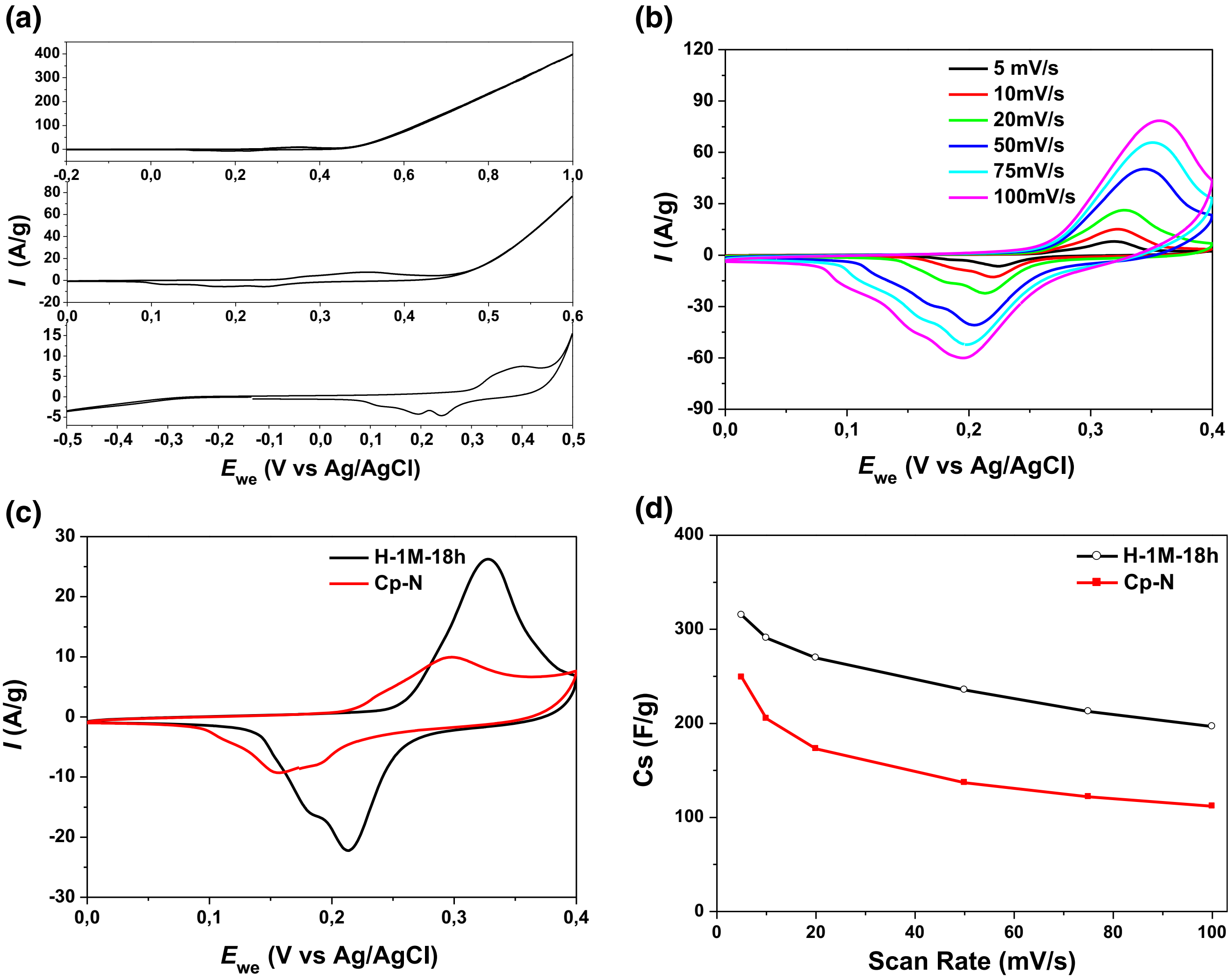

Fig. 6 **a** Cyclic voltammograms in 6 M KOH electrolyte of the H-1M-18h sample at different potential ranges for 20 mV/s. **b** CV curves of the H-1M-18h sample at different scan rates. **c** Comparative CV curves of Cp-N and H-1M-18h samples at 20 mV/s. **d** Variation of specific capacitances vs. scan rate for co-precipitation and hydrothermal $CoFe_2O_4$ products

Table 2 Specific capacitance of some spinel oxides depending on the synthesis method, electrolyte, and position of our results

Electroactive material	Synthesis method	Electrolyte		Cs (F/g)	Ref.
$CoFe_2O_4$	Co-precipitation	0.5 M Na_2SO_4	18.7	(5 mA/cm^2)	[50]
$CoFe_2O_4$	Hydrothermal	1 M KOH	52.5	(1 mV/s)	[51]
$CoFe_2O_4$	Electrodeposition	1 M NaOH	366	(5 mV/s)	[13]
$CoFe_2O_4$	Combustion	1 M KOH	356	(1 mA/cm^2)	[52]
$CoFe_2O_4$/FeOOH composite	One-pot hydrothermal	6 M KOH	332.4	(0.5 A/g)	[15]
Fe_3O_4	Hydrothermal	1 M Na_2SO_4	207.7	(0.4 A/g)	[53]
Mn_3O_4	Hydrothermal	1 M Na_2SO_4	348	(0.5 A/cm^2)	[54]
$ZnCo_2O_4$	Co-precipitation	6 M KOH	77	(5 mV/s)	[55]
Mn_3O_4	Microwave-assisted reflux	6 M KOH	94	–	[56]
$MnCo_2O_4$	D-Glucose-assisted solvothermal process	6 M KOH	346	(1 A/g)	[57]
$CoFe_2O_4$	Co-precipitation Hydrothermal	6 M KOH	**295** **429**	(0.5 A/g) (0.5 A/g)	This work

nanocrystalline and mesoporous nature of our $CoFe_2O_4$ MNPs. It is to be noted that background capacitances of Ni and carbon black (that only serves as conductive additive) and the non-conductive binder are negligible, as proven previously in [11], where the same Ni foam was used. According to Fig. 6d, C_s decreased gradually from 315 to 197 F/g and from 249 to 112 F/g for H-1M-18h and Cp-N samples, respectively, as the scan rates increased from 5 to 100 mV/s. This is attributed to the fact that the electrolyte ions can only access to the outer region of the pores at high scan rates [58].

Figure 7a shows the galvanostatic charge–discharge curves of the as-prepared electrode H-1M-18h in the potential range of 0–0.4 V at various current densities from 1 to 10 A/g. The non-linear plot reveals the presence of a faradaic nature of the electrode material.

The C_s (in F/g) of the electrodes was calculated according to the corresponding galvanostatic discharge curves using the following equation:

$$C_s = \frac{i \times \Delta t}{m \Delta V} \tag{2}$$

where i is the current (A), Δt is the discharge time (s), m is the active material loading mass (g), and ΔV is the potential window (V). The variations of the specific capacitance with the current density of these electro-active materials are displayed in Fig. 7b. The specific capacitances for the two samples decrease gradually as the current density is increased. At 0.5 A/g, a maximum specific capacitance value of 429 and 295 F/g was recorded for the H-1M-18h and Cp-N samples, respectively. These values are higher than those obtained in literature for other spinel oxides [13, 15, 50–57] (see Table 2) and are attributed to the promising electrochemical performance of the nanoferrites. Moreover, the electrodes still maintain a significant specific capacitance values even at high current densities, i.e., 250 F/g at 10 A/g for the H-1M-18h electrode. Recently, Laheäär et al. [59] stated that for such metal oxides involving charge transfer reactions, and because of the non-linearity of GCD curves, the evaluation of specific capacitance should not be done from discharge time utilizing Eq. (2) as for electrical double-layer capacitors (EDLCs). To avoid an eventual over-/under-estimation of capacitive performance, specific capacitance in farad per gram has also been obtained from the specific integrated discharge energy $E_{s,int/D}$ according to the following equations:

$$C_{s,int/D} = \frac{2\,E_{int/D}}{\Delta V^2} \tag{3}$$

where $E_{int/D}$ is calculated by integrating the galvanostatic discharge curve:

$$E_{s,int/D} = \frac{i}{m} \int_{t(U_{max})}^{t(U_{min})} U(t)dt \tag{4}$$

Here, i is the current (A), m is the active material loading mass (g), and ΔV is the potential window (V).

At a current of 0.5 A/g, maximum values of specific capacitance, $C_{s,int/D}$ = 481 and 299 F/g, have been obtained for H-1M-18h and Cp-N samples, respectively. These values are larger than the ones obtained from Eq. (2), which means that those were not underestimated.

Values of the specific energy $E_{s,int/D}$ in units (Wh/kg) obtained for H-1M-18h and Cp-N samples are 10.68 and 5.48 Wh/kg, respectively. The specific discharge capacity is also determined in milliampere hours per gram from the following equation:

$$Q_D = I^{\ddot{E}} t_D/3.6 \tag{5}$$

where t_D is the discharge time in seconds. The obtained values are 47.6 and 29.7 mAh/g for H-1M-18h and Cp-N samples, respectively. It is clear that the best values are obtained for the material made by the hydrothermal process.

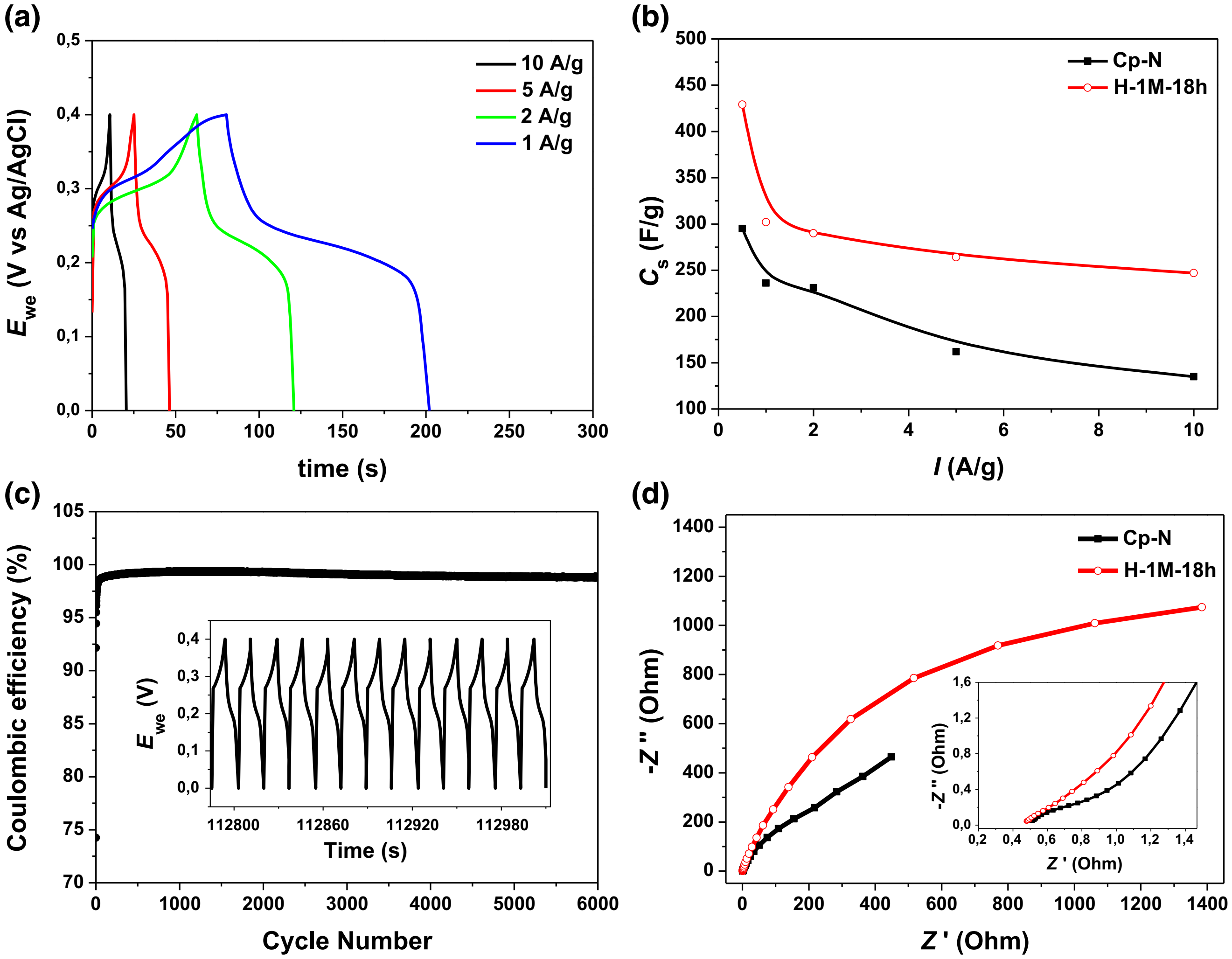

Fig. 7 **a** Galvanostatic charge/discharge curves at different current density of the H-1M-18h sample. **b** Specific capacitance variation vs. current density for H-1M-18h and Cp-N samples. **c** Cyclic stability at 10 A/g of the H-1M-18h sample. **d** Nyquist plot of H-1M-18h and Cp-N samples

It is worth noting that the best values obtained here are still a bit far from the theoretical value of 1028 F/g. This could be due to many factors such as the adherence of the material on the current collector and also to the intrinsic resistance of the material which is influenced by the growth technique.

The long-term cycling performance is another important factor in determining supercapacitor electrode performances for energy storage application.

Figure 7c shows the electrochemical and cyclic stability of the H-1M-18h electrode at a current density of 10 A/g. The coulombic efficiency of the cobalt ferrite MNP-based electrode material after 6000 cycles is 98.8% which proves the excellent long-term stability for the electro-active electrode material. The charge-discharge curves of the last 19 cycles ending the cycling test are shown by the inset in Fig. 7c, and it is clear that there is no observable change in shape within the potential window of 0.0 to 0.4 V.

Figure 7d illustrates the Nyquist plots of H-1M-18h and Cp-N electrodes before cycling with the inset to the figure showing the expanded high-frequency region of the same plot. In the high-frequency region, the intercept with real part (Z') represents the combined solution resistance (R_s) which includes the ionic resistance in the electrolyte, intrinsic resistance of substrate, and contact resistance at the active material/current collector [60]. The R_s values obtained are 0.50 and 0.47 Ω for the Cp-N and H-1M-18h electrodes, respectively. In the case of the Cp-N electrode, a semicircle at the high-frequency region is observed denoting the charge transfer resistance, R_{ct} which is estimated as 1.52 Ω (the diameter of this semicircle), and attests for a good electrode contact with the electrolyte [61].

In the low-frequency region, a straight line curve close to 45° with the Z' axis for the Cp-N electrode is observed, which is attributed to the Warburg impedance related to the diffusion/transport of counter ions between the electrolyte (KOH) and the pores of the electro-active material during the redox reactions. This implies that the Cp-N supercapacitor has a capacitive behavior at low frequencies whereas, for the H-1M-18h electrode, a noticeable deviation from the line is observed, which shows a more resistive behavior. Figure 8 shows the fitted EIS data of the Cp-N sample with the ZFIT/EC-lab program, version 10.44. In the corresponding equivalent circuit, R_1 represents the ionic charge transfer resistance (R_{ct}), R_2 is attributed to the electron transfer resistance, Q_1 and Q_2 are constant phase elements (CPE), and W_2 is a Warburg element.

Conclusion

$CoFe_2O_4$ spinel ferrite magnetic MNPs have been successively synthesized by two different methods "co-precipitation and hydrothermal process" using different Co and Fe precursors with different concentrations as well as growth conditions (time and temperature). The optimized condition for the co-precipitation method is the use of nitrate-based precursors under 80 °C reaction temperature, whereas there was no noticeable difference in results for the hydrothermally prepared samples. Microstructural analysis confirms the formation of the single-phase cubic spinel structure, and the morphological studies from FESEM and HRTEM micrographs demonstrate the formation of nanosized particles with an average particle size between 11 and 26 nm. The surface area and pore size distribution measurements reveal the presence of a mesoporous structure in these cobalt ferrite NPs with a surface area around 34 $m^2 g^{-1}$. Nanoparticles made by hydrothermal synthesis have a saturation magnetization of 63 emu/g and a coercivity of 750 Oe at room temperature. The electrochemical properties of these ferrites material prepared by the hydrothermal method reveals a superior faradaic type behavior, with a high specific capacitance of approximately 429 F/g at a current density of 0.5 A/g and excellent cycle life with a coulombic efficiency of 98.8% after 6000 cycles at a current density of 10 A/g. The results obtained demonstrate the adoption of the ferrite NPs as a promising material for supercapacitor applications.

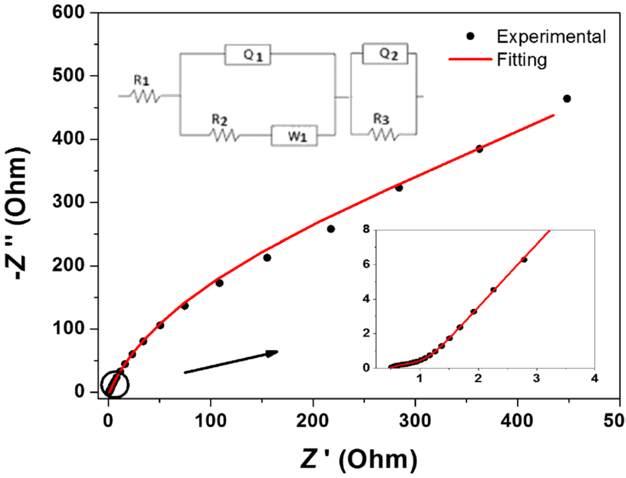

Fig. 8 EIS plot and fitting curve using the inset equivalent circuit for the Cp-N sample

Acknowledgements This work is based upon research supported by General Direction of Scientific Research and Technological Development (DGRSDT) via the Algerian Ministry of Higher Education and Scientific Research as well as the South African Research Chairs Initiative (SARChI) in Carbon Technology and Materials of the Department of Science and Technology (DST) and the National Research Foundation (NRF) through the Algeria/South Africa collaboration program. We are also grateful to Prof. A.M. Strydom for the magnetic characterization done with the use of the MPMS system at the Department of Physics, University of Johannesburg. H. Kennaz acknowledges support of the University of Annaba and DGRSDT for the financial assistance provided for his PhD study.

References

1. Raj K, Moskowitz R, Casciari R (1995) Advances in ferrofluid technology. J Magn Magn Mater 149:174–180
2. Gunther L (1990) Quantum tunnelling of magnetisation physics. Phys World 2:28
3. Mazaleyrat F, Varga LK (2000) Ferromagnetic nanocomposites. J Magn Magn Mater 215:253–259
4. Issa B, Obaidat IM, Albiss BA, Haik Y (2013) Magnetic nanoparticles: surface effects and properties related to biomedicine applications. Int J Mol Sci 14:21266–21305
5. Obreja VVN (2014) Supercapacitors specialities-Materials review. AIP Conf Proc 1597:98–120
6. Wang G, Zhang L, Zhang J (2012) A review of electrode materials for electrochemical supercapacitors. Chem Soc Rev 41:797–828
7. Li YH, Huang KL, Liu SK, Yao ZF, Zhuang SX (2011) J Solid State Electrochem 15:587–592
8. Zheng YZ, Ding HY, Zhang ML (2009) Mater Res Bull 44: 403–407
9. Song MS, Lee KM, Lee YR, Kim IY, Kim TW, Gunjakar JL, Hwang SJ (2010) Porously assembled 2D nanosheets of alkali metal manganese oxides with highly reversible pseudocapacitance behaviors. J Phys Chem C 114:22134–22140
10. Zhu M, Wang Y, Meng D, Qin XZ, Diao G (2012) Hydrothermal synthesis of hematite nanoparticles and their electrochemical properties. J Phys Chem C 116:16276–16285
11. Bello A, Makgopa K, Fabiane M, Dodoo-Ahrin D, Ozoemena KI, Manyala N (2013) Chemical adsorption of NiO nanostructures on nickel foam-graphene for supercapacitor applications. J Mater Sci 48:6707–6712
12. Bello A, Fashedemi OO, Fabiane M, Lekitima JN, Ozoemena KI, Manyala N (2013) Microwave assisted synthesis of MnO_2 on nickel foam-graphene for electrochemical capacitor. Electrochim Acta 114:48–53
13. Kumbhar VS, Jagadale AD, Shinde NM, Lokhande CD (2012) Chemical synthesis of spinel cobalt ferrite ($CoFe_2O_4$) nano-flakes for supercapacitor application. Appl Surf Sci 259:39–43
14. He P, Yang K, Wang W, Dong F, Du L, Deng Y (2013) Reduced graphene oxide-$CoFe_2O_4$ composites for supercapacitor electrode. Russ J Electrochem 49:359
15. Zhang YX, Hao XD, Diao ZP, Li J, Guan YM (2014) One-pot controllable synthesis of flower-like $CoFe_2O_4$/FeOOH nanocomposites for high-performance supercapacitors. J Mater Lett 123: 229–234

16. Adam JD, Krishnaswamy SV, Talisa SH, Yoo KC (1990) Thin-film ferrites for microwave and millimeter-wave applications. J Magn Mater 83:419–424
17. Lee JG, Park JY, Oh YJ, Kim CS (1998) Magnetic properties of $CoFe_2O_4$ thin films prepared by a sol-gel method. J Appl Phys 84(5):2801
18. Bao N, Shen L, Padhan P, Gupta A (2008) Self-assembly and magnetic properties of shape-controlled monodisperse $CoFe_2O_4$ nanocrystals. J Appl Phys Lett 92:173101
19. Pannaparayil T, Marande R, Komarneni S (1991) J Appl Phys 69: 5349–5351
20. Rozman M, Drofenik M (1995) Hydrothermal synthesis of manganese zinc ferrites. J Am Ceram Soc 78:2449–2455
21. Komarneni S, Fregeau E, Breval E, Roy R (1998) J Am Ceram Soc 71:26–28
22. Sisk M, Kilbride I, Barker AJ (1995) Production of manganese zinc ferrites via the hydrothermal decomposition of metal (III) acetates and citrates. J Mater Sci Lett 14:153–154
23. Shafi KVPM, Koltypin Y, Gedanken A, Prozorov R, Balogh J, Lendvai J, Felner IJ (1997) Sonochemical preparation of nanosized amorphous $NiFe_2O_4$ particles. J Phys Chem 101:6409–6414
24. Moumen N, Pileni MP (1996) New syntheses of cobalt ferrite particles in the range 2–5 nm: comparison of the magnetic properties of the nanosized particles in dispersed fluid or in powder form. J Chem Mater 8:1128–1134
25. Davis KJ, Wells S, Upadhayy RV, Charle SW, O'Grady KO, El Hilo M, Meaz T, Morup S (1995) J Magn Magn Mater 14:149
26. Grigorova M, Blythe HJ, Blaskov V, Rusanov V, Petkov V, Masheva V, Nihtianova D, Martinez LIM, Munoz JS, Mikhov M (1998) J Magn Magn Mater 163:193
27. Blaskov V, Petkov V, Rusanov V, Martinez LIM, Martinez B, Munoz JS, Mikhov M (1996) J Magn Magn Mater 162:331
28. Pham-Huu C, Keller N, Estournes C, Ehret G, Greneche JM, Ledoux MJ (2003) Microstructural investigation and magnetic properties of $CoFe_2O_4$ nanowires synthesized inside carbon nanotubes. J Phys Chem Chem Phys 5:3716
29. Hoh JC, Yaacob II (2002) Polymer matrix templated synthesis: cobalt ferrite nanoparticles preparation. J Mater Res 17:3105
30. Xinyong L, Kutal C (2003) Synthesis and characterization of superparamagnetic $Co_xFe_{3-x}O_4$ nanoparticles. J Alloys Compd 349:264–268
31. Lutterotti L, Matthies S, Wenk H (1999) MAUD: a friendly Java program for material analysis using diffraction. CPD NEWSLETTER 21:14–15
32. Qu Y, Yang H, Yang N, Fan Y, Zhu H, Zou G (2006) The effect of reaction temperature on the particle size, structure and magnetic properties of coprecipitated $CoFe_2O_4$ nanoparticles. J Mater Lett 60:3548–3552
33. Shenoy SD, Joy PA, Anantharaman MR (2004) Effect of mechanical milling on the structural, magnetic and dielectric properties of coprecipitated ultrafine zinc ferrite. J Magn Magn Mater 269:217
34. Hu G, Choi JH, Eom CB, Harris VG, Suzuki Y (2000) Structural tuning of the magnetic behavior in spinel-structure ferrite thin films. J Phys Rev 62:779
35. Ferreira TAS, Waerenborgh JC, Mendonça MHRM, Nunes MR, Costa FM (2003) Structural and morphological characterization of $FeCo_2O_4$ and $CoFe_2O_4$ spinels prepared by a coprecipitation method. J Solid State Sci 5:383–392
36. Le-Trong H, Barnabe A, Presmanes L, Tailhades P (2008) Phase decomposition study in $Co_xFe_{3-x}O_4$ iron cobaltites: synthesis and structural characterization of the spinodal transformation. J Solid State Sci 10:550–556
37. Rouquerol F, Rouquerol J, Sing K (1999) Adsorption by powders and porous solids: principles, methodology and applications, 1st edn. Academic Press, San Diego, 467 p
38. Yu T, Shen ZX, Shi Y, Ding J (2002) Cation migration and magnetic ordering in spinel $CoFe_2O_4$ powder: micro-Raman scattering study. J Phys Condens Matter 14:613
39. Wang ZW, Downs RT, Pischedda V, Shetty R, Saxena SK, Zha CS, Zhao YS (2003) High-pressure x-ray diffraction and Raman spectroscopic studies of the tetragonal spinel $CoFe_2O_4$. J Phys Rev 68: 094101
40. Ahmed MA, Ateia E, Salah LM, El-Gamal AA (2005) Structural and electrical studies on La^{3+} substituted Ni-Zn ferrites. J Mater Chem Phys 92:310–321
41. Waldron RD (1955) Infrared spectra of ferrites. J Phys Rev 99: 1727–1735
42. Li M, Mao Y, Yang H, Li W, Wang C, Liu P, Tong Y (2013) Controllable electrochemical synthesis of $CoFe_2O_4$ nanostructures on FTO substrate and their magnetic properties. New J Chem 37: 3116–3120
43. Liu C, Rondinone AJ, Zhang ZJ (2000) Synthesis of magnetic spinel ferrite $CoFe_2O_4$ nanoparticles from ferric salt and characterization of the size-dependent superparamagnetic properties. J Pure Appl Chem 72:37
44. Kolhatkar AG, Jamison AC, Litvinov D, Willson RC, Lee TR (2013) Tuning the magnetic properties of nanoparticles. Int J Mol Sci 14:15977–16009
45. Poddar P, Gass J, Rebar DJ, Srinath S, Srikanth H, Morrison SA, Carpenter EE (2006) Magnetocaloric effect in ferrite nanoparticles. J Magn Magn Mater 307:227–231
46. Peddis D, Cannas C, Musinu A, Piccaluga G (2009) Magnetism in nanoparticles: beyond the effect of particle size. J Chem Eur 15: 7822–7829
47. Du Tremolet de Lacheisserie E et Al (2000) Magnétisme I-Fondements. EDP Sciences, France
48. Goh SC, Chia CH, Zakaria S, Yusoff M, Haw CY, Ahmadi S, Huang NM, Lim HN (2010) Hydrothermal preparation of high saturation magnetization and coercivity cobalt ferrite nanocrystals without subsequent calcination. J Mater Chem Phys 120:31–35
49. Rao KS, Choudary GSVRK, Rao KH, Sujathad C (2015) Procedia Mater Sci 10:19–27
50. He P, Yang K, Wang W, Dong F, Du L, Deng Y (2013) Reduced graphene oxide-$CoFe_2O_4$ composites for supercapacitor electrode. J Electrochem 49(4):359–364
51. Xiong P, Huang H, Wang X (2014) Design and synthesis of ternary cobalt ferrite/graphene/polyaniline hierarchical nanocomposites for high- performance supercapacitors. J Power Sources 245:937–946
52. Umeshbabu E, Rajeshkhanna G, Rao GR (2014) Urchin and sheaf-like $NiCo_2O_4$ nanostructures: synthesis and electrochemical energy storage application. Int J Hydrogen Energy 39:15627–15638
53. Laheäär A, Przygocki P, Abbas Q, Béguin F (2015) Appropriate methods for evaluating the efficiency and capacitive behavior of different types of supercapacitors. Electrochem Commun 60:21–25
54. Bruke A (2000) Ultracapacitors: why, how, and where is the technology. J Power Sources 91:37
55. Portet C, Lillo-Rodenas MA, Linares-Solano A, Gogotsi Y (2009) Capacitance of KOH activated carbide-derived carbons. J Phys Chem Chem Phys 11:4943–4945
56. Shanmugavani A, Kalpana D, KalaiSelvan R (2015) Electrochemical properties of $CoFe_2O_4$ nanoparticles as negative and $Co(OH)_2$ and $Co_2Fe(CN)_6$ as positive electrodes for supercapacitors. J Mater Res Bull 71:133–141
57. Wang L, Ji H, Wang S, Kong L, Jiang X, Yang G (2013) Preparation of Fe_3O_4 with high specific surface area and improved capacitance as a supercapacitor. J Nanoscale 5:3793
58. Shaik DP, Rosaiah P, Hussain OM (2015) Enhanced supercapacitive performance of nanocrystalline Mn_3O_4 synthesized by hydrothermal method. J Advances in Chemistry 12(1): 3919–3933

59. Karthikeyan K, Kalpana D, Renganathan NG (2009) Synthesis and characterization of $ZnCo_2O_4$ nanomaterial for symmetric supercapacitor applications. J Ionics 15:107–110
60. Sankar KV, Kalpana D, Selvan RK (2012) Electrochemical properties of microwave-assisted reflux-synthesized Mn_3O_4 nanoparticles in different electrolytes for supercapacitor applications. J Appl Electrochem 42:463–470
61. Padmanathan N, Selladurai S (2014) Mesoporous $MnCo_2O_4$ spinel oxide nanostructure synthesized by solvothermal technique for supercapacitor. J Ionics 20:479–487